Article:
Qi, J. orcid.org/0000-0001-5235-0027, Ma, L., Gong, P. et al. (1 more author) (2023) Investigation of the wear transition in CoCrMo alloys after heat treatment to produce an HCP structure. Wear, 518-519. 204649. ISSN: 0043-1648

https://doi.org/10.1016/j.wear.2023.204649

Wear 518-519 (2023) 204649

Contents lists available at ScienceDirect

Wear

journal homepage: www.elsevier.com/locate/wear

Investigation of the wear transition in CoCrMo alloys after heat treatment to produce an HCP structure

J. Qi, L. Ma, P. Gong, W.M. Rainforth *

Department of Material Science and Engineering, The University of Sheffield, Sheffield, S1 3JD, UK

ARTICLE INFO

Keywords:
Wear transition
σ-CoCr
Heat treatment
TEM
PeakForce QNM
PED

ABSTRACT

This study reports that the wear rate of the heat-treated CoCrMo alloy shows a sudden transition of more than 5-fold when the load/contact pressure increases from 45 N (3.6 GPa) to 50 N (3.7 GPa). Heat treatment was used to change the structure of the commercially available CoCrMo from the initial face-centred cubic (γ-fcc) with a small amount of hexagonal close-packed (ε-hcp) to predominantly hcp ε-phase with dispersed nanoscale precipitates of σ-phase. PeakForce QNM was used to quantitatively map the local mechanical properties of the surface at the nanoscale. High-resolution transmission electron microscopy (HRTEM), scanning transmission electron microscope (STEM), energy-dispersive X-ray spectroscopy (EDX), and precession electron diffraction (PED) integrated with the TEM is used to characterize the structure and chemical composition of the worn surface and tribofilm. The possible reason for wear transition was discussed.

1. Introduction

Cobalt-based alloys have been widely used as surgical implant materials for decades because of their excellent biocompatibility and wear resistance [1,2]. The equilibrium structure of Co–Cr alloy above approximately 900–950 °C is face-centred cubic (fcc) γ-phase, and below it is hexagonal close-packed (hcp) ε-phase [3]. The transformation temperature varies depending on the exact composition. The ability of CoCrMo alloys to fully transform from fcc to hcp phase at room temperature is sluggish and suppressed due to the presence of a significant amount of alloying elements. Consequently, the alloys usually maintain a metastable γ-fcc matrix which co-exists with a small amount of ε-hcp at room temperature. The presence of two different lattices creates obstacles to the movement of dislocations and thus induces strengthening [1,3]. Solution treatment has been used to homogenise the microstructure, dissolve some of the carbides into the matrix and improve the strength, ductility and fatigue life, especially for the as-cast alloys [4–8]. Detailed reviews can be found elsewhere [9,10]. The annealing temperature of 1230 ± 5 °C, followed by isothermal aging at 850 °C, is often used for low carbon CoCrMo [4,5,7,11]. The volume fraction of hcp phase increases with the isothermal time [6,8,11]. However, sometimes the transformation to hcp did not go to completion even after holding up to 40 h [12]. Therefore, a longer isothermal time is required to achieve a high volume fraction of the hcp phase.

There are a number of reports on the effect of heat treatment of CoCr based alloys on the wear behaviour. Khaimanee et al. [13] heat treated CoCrMo to develop a hcp matrix structure. They found that the hcp structure offers better wear resistance than the fcc structure. The heat treated structures they report clearly contain σ-phase, an inevitable result of heat treatment, but they did not comment on the effect of this phase on wear. Moreover, only one load, 2 N, was investigated. Similarly, Zangeneh et al. [4] used heat treatment to transform the fcc structure to hcp. The heat treatment also resulted in the precipitation of a large volume fraction of $M_{23}C_6$. They showed that at low load the hcp structure gave the lowest wear rates, while at the highest loads the fcc structure gave the lower wear rate, where delamination was observed in the hcp structure. However, the wear was dominated by the role of the surface oxide film, making it difficult to interpret the role of the phase constitution. The role of carbide has been investigated by Cawley et al. [14] and Liao et al. [15], with the effect on wear being complex. Zhao et al. [16] have examined the wear behaviour of an ultra-fine grained Co–30%Cr alloy that also contained nanoscale σ-phase and found excellent wear behaviour, but it was not clear whether this was a result of the nanoscale structure (both hcp and σ-phase) or the phase constitution. Saldívar-García and López suggested that the hip implant prototypes with fully hcp matrix microstructures should be considered on the basis that they can offer low wear rates on contact [6]. However, there has not been any study that investigates whether the hcp structure

* Corresponding author.
E-mail address: m.rainforth@sheffield.ac.uk (W.M. Rainforth).

https://doi.org/10.1016/j.wear.2023.204649
Received 18 October 2022; Received in revised form 1 February 2023; Accepted 2 February 2023
Available online 4 February 2023

offers better or worse wear behaviour over a range of loads. Therefore, this study seeks to answer that question using the same conditions that were used to investigate the standard fcc CoCrMo alloys [2].

The impacts of hard phases such as carbides ($M_{23}C_6$ and M_7C_3, M = Co, Cr or Mo) and intermetallic compounds (Cr_8Co_7, Co_9Mo_{15}) on the tribological performance of CoCrMo were extensively investigated in retrieval and in vitro studies [15–17]. The carbide and σ-phase precipitations are difficult to avoid since most hot working and heat treatments take place below the transformation temperature [18–20]. σ-Precipitation was reported to enhance the hardness and, at the same time, decrease the impact value of the duplex stainless steel drastically and deteriorate the corrosion properties since Mo and Cr accumulate in the σ phase [21–24]. Chen et al. [25] investigated the synergy effects of the σ-phase and carbide on the wear behaviour of γ-phase dominated low- (LC) and high-carbon (HC) CoCrMo alloys in Hanks' solution. It was found that fractured σ-phase precipitates were the main reason for abrasion for both LC and HC alloys. Carbides were "torn off" at the initial high contact pressure resulting in surface pitting; the σ-phase precipitates around the pits were uprooted and led to micro-cracks, which were considered to result in surface fatigue of the HC alloy. In contrast, strain-induced martensite observed on the worn surface contributed to the increase of hardness and abrasion resistance of the LC alloy.

Although the increase of hardness with the existence of σ-phase is undoubtable, the wear and corrosion behaviour of the hcp ε-phase dominant CoCrMo with σ-precipitates has not been thoroughly investigated, especially under the condition of high contact pressure and without carbides. This paper reveals the impact of σ-phase on the wear and corrosion performance of ε-phase CoCrMo under high load/contact pressure. σ-Phase was characterized by EDX, HRTEM, and TEM integrated precession electron diffraction (PED). The modulus of the σ-phase was measured by PeakForce QNM (PF_QNM) by AFM.

2. Experimental procedures

2.1. Material and preparation

Commercially available cast CoCrMo alloy bar (13 mm dia.) was sectioned into 5 mm thick discs before heat treatment. The sample discs were then heated to 1230 °C and held for 3 h, followed by a water-quench to 850 °C, then held at 850 °C for 120 h. The long isothermal ageing time of 120 h is used to ensure the completion of the transformation and maximise the volume fraction of the hcp phase. The chemical composition of the sample before heat treatment can be found elsewhere [2]. All samples after heat treatment were mechanically ground, polished and washed before the tribocorrosion tests following the methods described elsewhere [2].

2.2. Wear testing

The ball on disc reciprocating tribocorrosion tests (conformed to ASTM G133) were carried out on a Bruker UMT TriboLab system (Bruker, UK). The details of the tests are reported elsewhere [2]. The counterface was a 5 mm diameter alumina ball (99% purity; Oakwase Ltd., UK). An alumina ball was used because an inert counterpart is required. A wide range of normal loads were used, namely 5 N, 20 N, 30 N, 40 N, 45 N, 50 N and 70 N. The test was repeated three times for each load, and the results were found to be consistent. The initial maximum contact pressures were calculated using the Hertzian equations [2] and are presented in Fig. 1.

The wear volume was measured using an optical Dektak® 150 profilometer (Bruker, UK). The wear rate is then calculated by the standard formula:

$$K = \frac{V}{S}$$

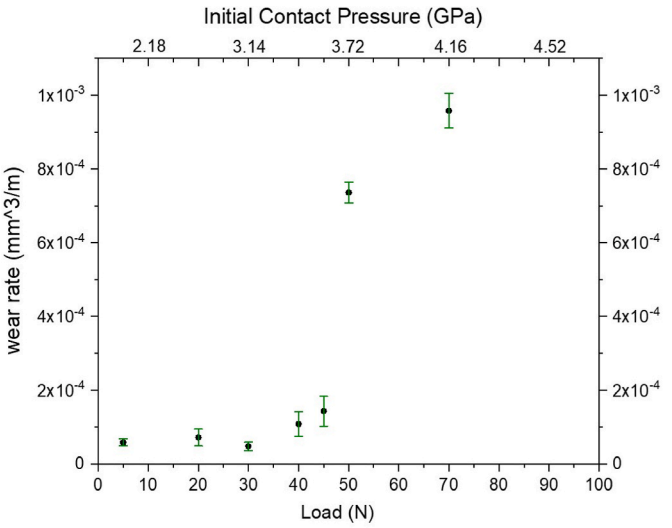

Fig. 1. Wear rate plot against load and initial contact pressure.

Where K is the specific were rate in units of mm^3/m, V is the wear volume in mm^3, and S is the total sliding distance in m.

2.3. Characterization of the surface and subsurface

2.3.1. XRD

XRD results were acquired on a D2 Phaser (Bruker, UK) using Cu-Kα radiation at an angle (2θ) ranging from 30° to 100°. The step size is 0.1. XRD data was processed by DIFFRAC.EVA software (Bruker).

2.3.2. SEM and EBSD

SEM, EDX and EBSD data were collected by an FEI Nova NanoSEM 450 operated at 20 kV, and a JEOL JEM 7900 F operated at 30 kV with various step sizes comparable to the scan size. AztecCrystal (Oxford Instruments, UK) was used for data process and analysis.

2.3.3. Surface hardness and micro/nano-mechanical test

The Vickers hardness of the bulk materials before and after the heat treatment was measured using a Durascan D5 (EMCO-TEST, Austria). About 10 test sites were randomly selected on each surface, and the mean value was calculated as the hardness of the bulk material.

Nanoindentation (Hysitron, TI Premier, USA) was used to measure the mechanical properties of the sample surface after the heat treatment and worn surfaces. A Berkovich three-sided pyramidal indenter was used, with a 65.3 face angle. Data was output as.txt files and processed by OriginPro 2020b (Academic, OriginLab Corporation) following the standard procedure [2,26].

The PF_QNM was performed on a Bruker Dimension XR™ (Bruker, UK). A DNISP-HS (S/N 27,985,414, Bruker, UK) hand-crafted ultra-high force natural diamond Nanoindenting cantilever was used for PF_QNM measurement. The DNISP-HS used for mechanical property measurement has a nominal tip radius of 40 nm and a nominal spring constant of 400 N/M. It was calibrated by following the standard procedure from Bruker [27,28]. The measured modulus was calculated by NanoScope Analysis 2.0 (Bruker). JKR full model was chosen as the modulus fit model with a goodness of fit, $R^2 > 0.98$. Bruker's Sharp Nitride Lever (SNL, Bruker, UK) with a tip radius of ~2 nm was used for imaging and locating the testing area before the QNM measurement.

2.3.4. FBI sample preparation, TEM and NanoMegas measurement

The cross-sectional samples for triblayer and subsurface analysis and characterization were prepared by using a FEI Helios Focus Ion Beam (FIB). The structure and chemical composition of the interface, tribolayer and the subsurface were examined by a cold field emission gun (c-

FEG) JEOL F200 transmission electron microscope (TEM) coupled with a twin, solid-state, ultra-sensitive large silicon drift detectors (SDD) energy dispersive X-ray spectrometry (EDX) system operating at 200 kV.

The NanoMegas STAR™ precession electron diffraction (PED) and ASTAR™ ACOM-TEM systems, integrated with the JEOL F200 TEM, were used to acquire the phase and crystal orientation information of the subsurface beneath the worm surface. A precession angle of 0.7° was configured for all experiments. The precession frequency of 100 Hz and beam spot size of 10 nm were used. The step size of 2.5 nm for both x and y directions was used in all samples. The diffraction patterns were collected at a camera length of 150 nm. Once collected, the dataset was matched against simulated diffraction patterns and indexed automatically by Index software (NanoMegas, Belgium).

3. Results

3.1. Wear rate and tribo-corrosion results

The wear of the alumina counterface was not measurable. Indeed, no damage was observed. Therefore, the wear data reported only relates to the CoCrMo disc. The calculated wear rate was plotted against the load (lower x-axis) and initial maximum contact pressure (upper x-axis) in Fig. 1. The wear rate is relatively stable with load/pressure till 45 N (3.6 GPa). It suddenly increases more than 5-fold from 1.43×10^{-4} mm^3/m at 45 N (3.6 GPa) to 7.36×10^{-4} mm^3/m at 50 N (3.7 GPa), then to 9.58×10^{-4} mm^3/m at 70 N (4.2 GPa). The wear transition is pronounced.

Fig. 2A and B shows the friction coefficient (CoF) and open circle potential (OCP) change with time under different loads. CoFs for the loads below 50 N are relatively stable, around 0.08 to 0.1. When reaching 50 and 70 N, the CoFs are noisier than those at lower loads. At 50 N, the CoF is stable but at a relatively higher number (approximately 0.18) after early fluctuations. The CoF at 70 N decreases gradually from 0.25 at the running-in stage to 0.1, where it stables around after 1-h sliding. The CoF at 70 N is the noisiest one out of all. The mean COFs are summarised and shown in Fig. 2C. A sudden increase in mean COF from 0.08208 at 45 N to 0.1199 at 50 N is also observed.

The OCPs for lower loads (under 50 N) fluctuate around −0.35 V, except at 30 N, which is stable around −0.2 V after a brief drop. The OCP at 50 N drops to −0.55 V after the running-in, then gradually climbs up and stabilises at −0.35 V with significant fluctuations. At 70 N, OCP drops to −0.59 V at the running-in stage and quickly returns to around −0.48 V. It rises to 0.41 in about 40 min, followed by a sudden jump to −0.37 V. It slowly climbs back to the range of −0.25 to −0.3 V towards the end.

3.2. Material characterization of CoCrMo alloy after the heat-treatment

3.2.1. Phase identification

It is important to identify the end product due to the uncertainty of

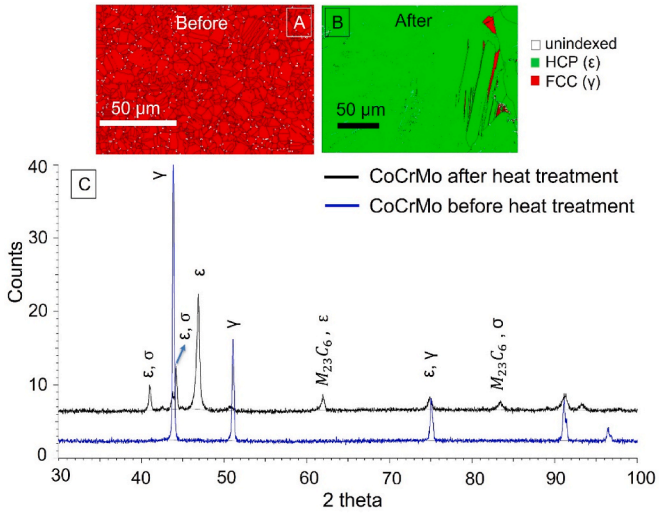

Fig. 3. XRD data for CoCrMo alloys before (blue) and after (black) the heat treatment. The possible phases are labelled above each peak. The insets are the EBSD maps for the surfaces for before (left) and after (right) heat treatment. (For interpretation of the references to colour in this figure legend, the reader is referred to the Web version of this article.)

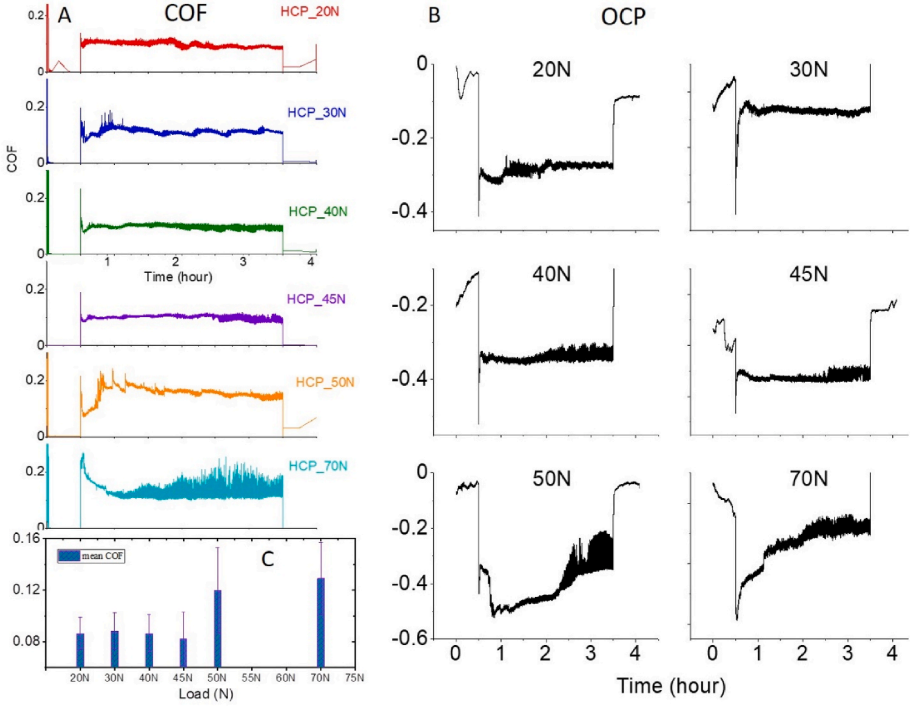

Fig. 2. A) CoF and B) OCP change with time and C) Mean CoFs under different loads.

the phase transformation after heat treatment. Fig. 3 shows the XRD spectra of CoCrMo alloys before (blue) and after (black) the heat treatment. The possible phases are labelled above the peaks according to the identification results. The insets are the EBSD phase maps with grain boundaries (GB) for before (left) and after (right) heat treatment. Before the heat treatment the alloy was dominated by the fcc (red) phase. After the heat treatment, it had transformed to the hcp (green) phase with a small amount of fcc phase still present and possibly $Cr_{23}C_6$ (00-035-0783) and σ-CoCr [29,30]. There were several peak overlaps (hcp and σ-CoCr, carbides and σ -CoCr). Therefore, it is difficult to uniquely resolve the phases solely from this XRD data. The inset EBSD phase maps confirm that before the heat treatment the microstructure is γ-CoCr, and after heat treatment it transformed to ε-CoCr with a small amount of γ-CoCr. No carbides or σ-CoCr were detected. This might be due to the big step size used in data collection, or the amount of carbides and σ-CoCr is not enough to be detected. It is also seen that the grain size is far bigger after heat treatment than before.

3.2.2. *Mechanical properties of the surfaces before and after wear tests*

The mechanical properties of the surfaces before and after tribo-corrosion tests under various loads were measured using nano-indentation. Following the standard procedure [2], the hardness (H) and reduced modulus (Er) are extracted and plotted in Fig. 4. The average was taken from 20 data points collected on the worn surface along the middle of the wear track in the direction of sliding with a 5 μm interval. The average of the unworn surface was taken from 220 indents randomly selected across the sample surface. There are marginal differences in hardness between the unworn surface and worn surfaces from different loads if the substantial hardness variation is taken into consideration.

Fig. 5 shows the surface morphology, phase map superimposed with GB, and the hardness distribution measured by the nanoindentation on a 75 μm × 75 μm region on the unworn surface after heat treatment. An array of 15 × 15 = 225 points data with a 5 μm interval were collected, as indicated by the black box in Fig. 5A and B. The hardness and modulus are not homogeneously distributed across the sample surface, as shown in Fig. 5C. Most of the region has a hardness of around 20 GPa. However, some locations have high values of up to 35 GPa, while many others are lower than 5 GPa.

Fig. 6 shows the hardness and phase map on the same surface in a relatively small region (20 μm × 25 μm). A 4 × 5 array of 20 indentation marks were made with a 5 μm interval (Fig. 6A). The black boxes in the SEM image and phase map (Fig. 6A and D) denote the indentation region. Note that the σ -CoCr has been identified in the EBSD phase map

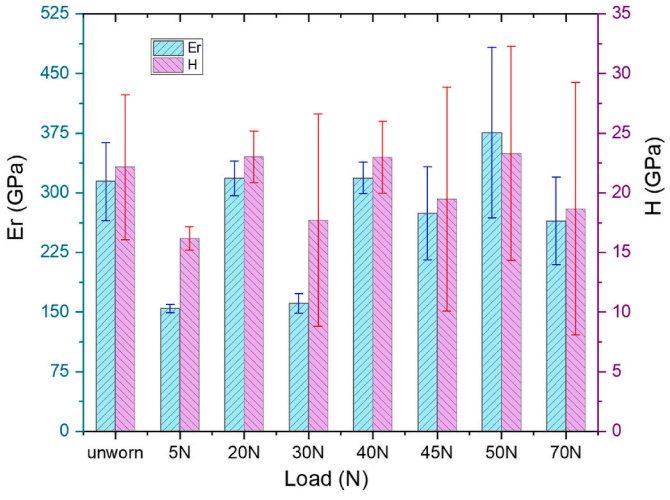

Fig. 4. Calculated hardness (H) and reduced modulus (Er) of the unworn and worn surfaces from different testing conditions.

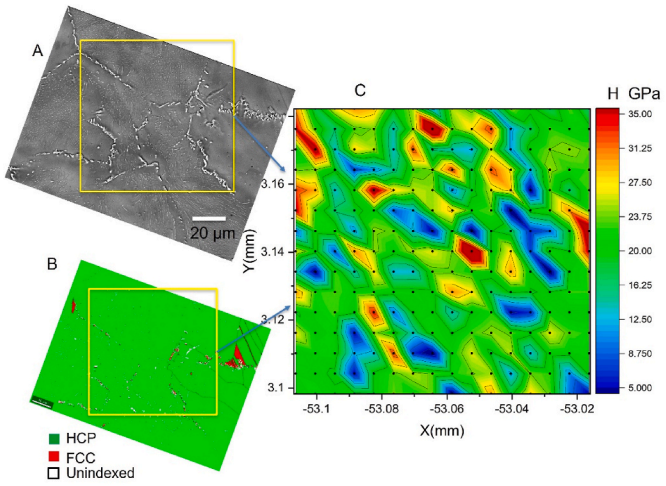

Fig. 5. A) SEM image of surface morphology; B) phase map with GB. The black boxes indicate the indentation area. C) The hardness map of the indentation area.

(Fig. 6D, blue dots, some were marked by the yellow circles), but no carbides ($M_{23}C_6$) are identified. Furthermore, the σ-CoCr is more often distributed in the region of the hcp phase or around the boundaries between ε and γ. This means the σ-CoCr forms during the heat treatment due to phase transformation and is not pre-existing in the starting material. The coloured hardness map (Fig. 6B) shows the surface hardness distribution. When comparing with the phase map (Fig. 6D) one can see that the region of green ε-hcp with σ blue dots has relatively high hardness values with small and shallow indent imprints (Fig. 6A), and the area with red γ-fcc phase is relatively soft, with deep and noticeable indent markers (Fig. 6A). The blue σ-phase dots closely marked the same region of the bright strips in Fig. 6A and C. The AFM image (Fig. 6C) visibly shows that the bright stripes protrude above the surface with a height of 20–40 nm. This strongly suggests that the bright strips are the σ-phase, and it was confirmed and will discuss in detail from the TEM and EDX data in the following sections. The yellow boxes in Fig. 6A and C indicate the PF_QNM measurement region in Fig. 7.

To investigate the mechanical properties of the stripes exhibiting bright contrast in Fig. 6C, PF_QNM was performed in the area indicated by the yellow boxes in Fig. 6A and C. The sample surface was briefly cleaned by electrochemical polishing for 5s to remove the oxide layer on the surface. The sample was then kept in methanol before the QNM measurement. An SNL cantilever was used to image the surface to locate the nano-indented area (Fig. 6C) at the scan rate of 2 Hz, scan size 30 μm × 30 μm with 512 × 512 pixels. Once the target region was identified, a DNISP_HS cantilever was used for PF_QNM measurement. A small area (5 μm × 5 μm, 256 × 256 pixels) in the selected region with both the bright stripe and partial nanoindentation mark was scanned under PF-QNM mode at a scan rate of 0.5 Hz. The actual tip radius was determined by following the standard procedure as mentioned previously as 42 nm, and deflection sensitivity was 69.3 nm/V. A high modulation frequency of 2 kHz (0.5 ms for the force curve) was used. The Peak Force setpoint was set at 0.5 μN, and the Peak Force Amplitude was 80 nm to ensure the indentation was comparable to cantilever deflection. Fig. 7 shows the scanned height image and calculated modulus map. The red arrows indicate the white stripe structures observed on the surface, and the white arrows indicate the indentation mark. The white stripe structures are above the surface level, as seen in Fig. 6C, about 10–30 nm. The indentation mark obviously shows a pit on the surface, a dark area on the height map (Fig. 7A). On the modulus map (Fig. 7B), both the white stripe structure and the indentation mark have a higher modulus than the substrate (250–300 GP). Furthermore, the white stripes have a relatively high modulus (above 700 GP) than other

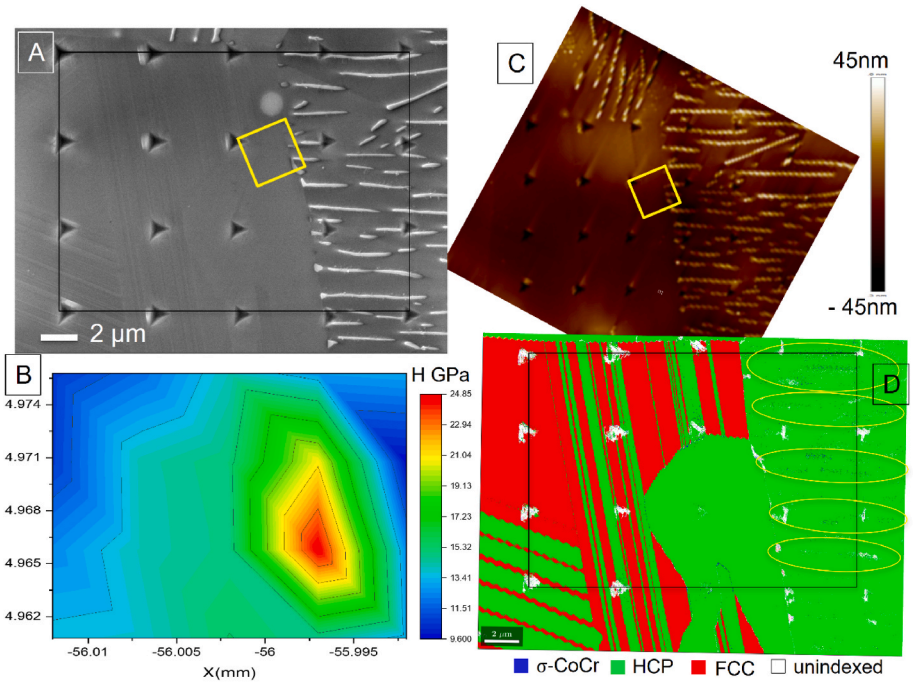

Fig. 6. SEM image with the black box indicating the nanoindentation area (A), the hardness distribution (B), the AFM image (C) and the phase map of the same region (D) on the heat-treated sample. The yellow boxes in A and C indicate the PeakForce QNM region in Fig. 7. (For interpretation of the references to colour in this figure legend, the reader is referred to the Web version of this article.)

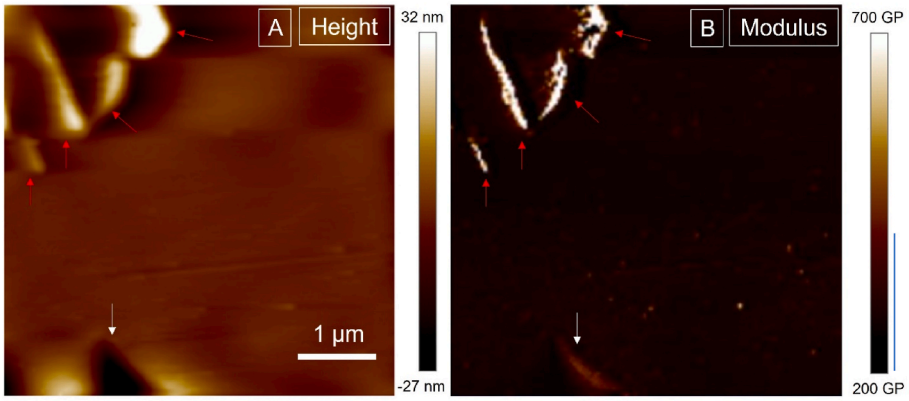

Fig. 7. PeakForce QNM result. AFM Height image (A) and Modulus map (B) of the area indicated in the yellow box in Fig. 6A&C. White arrow indicates the indentation mark, and red arrows indicate the elongated stripes in Fig. 6A and B. (For interpretation of the references to colour in this figure legend, the reader is referred to the Web version of this article.)

structures on the surface.

3.3. Characterization of the worn surfaces and subsurfaces

Fig. 8A–C shows the general morphology of the wear tracks of the 30 N, 45 N and 50 N tests. The worn surfaces are relatively smooth, with some scattered wear debris, especially for the 30 N sample (Fig. 8A). For the 45 N sample, cracks and cuts were occasionally found on the smooth wear track. The inset Fig. 8B shows one big crack (orange box in Fig. 8B) found in the middle of the 45 N wear track. The width of the wear track at 30 N and 40 N are the same (both are 510 μm), and only half of the width of the 50 N sample (c.a. 988 μm in Fig. 8B), with continuous grooves and cuts. This is consistent with the wear transition data, where the wear rate jumped approximately five times between 45 N and 50 N.

The microstructure of the subsurface under the worn surface from 30 N, 45 N and 50 N are shown in Fig. 8D, F and F, respectively. Fig. 8 G-K are the enlarged area for the red boxes in Fig. 8D–F. The FIB cross-sectional samples are taken in the middle of the wear tracks along the sliding direction. A layer of Pt deposition was laid on the top of the worn surfaces to protect them during the sample preparation, as shown by the white arrows in Fig. 8D–F.

All three FIB sections consist of lamellae which might be the recrystallization twins and are often observed in such samples. An unusual observation is the finger-like or elongated features distributed regularly across all sections, as indicated by the yellow arrows in Fig. 8D–K. These are identified later. The nanocrystalline layer can be seen in all three samples. The thickness of the nanocrystalline layer increases with the load. The size of the subgrains in the nanocrystalline layer gradually rises from the surface towards the bulk substrate, with the finest ones appearing at the top (Figs. 8 and 9). However, an abrupt interface between the nanocrystalline layer and the substrate (marked by the red arrows in Fig. 8G–K) is observed, and it is more noticeable in

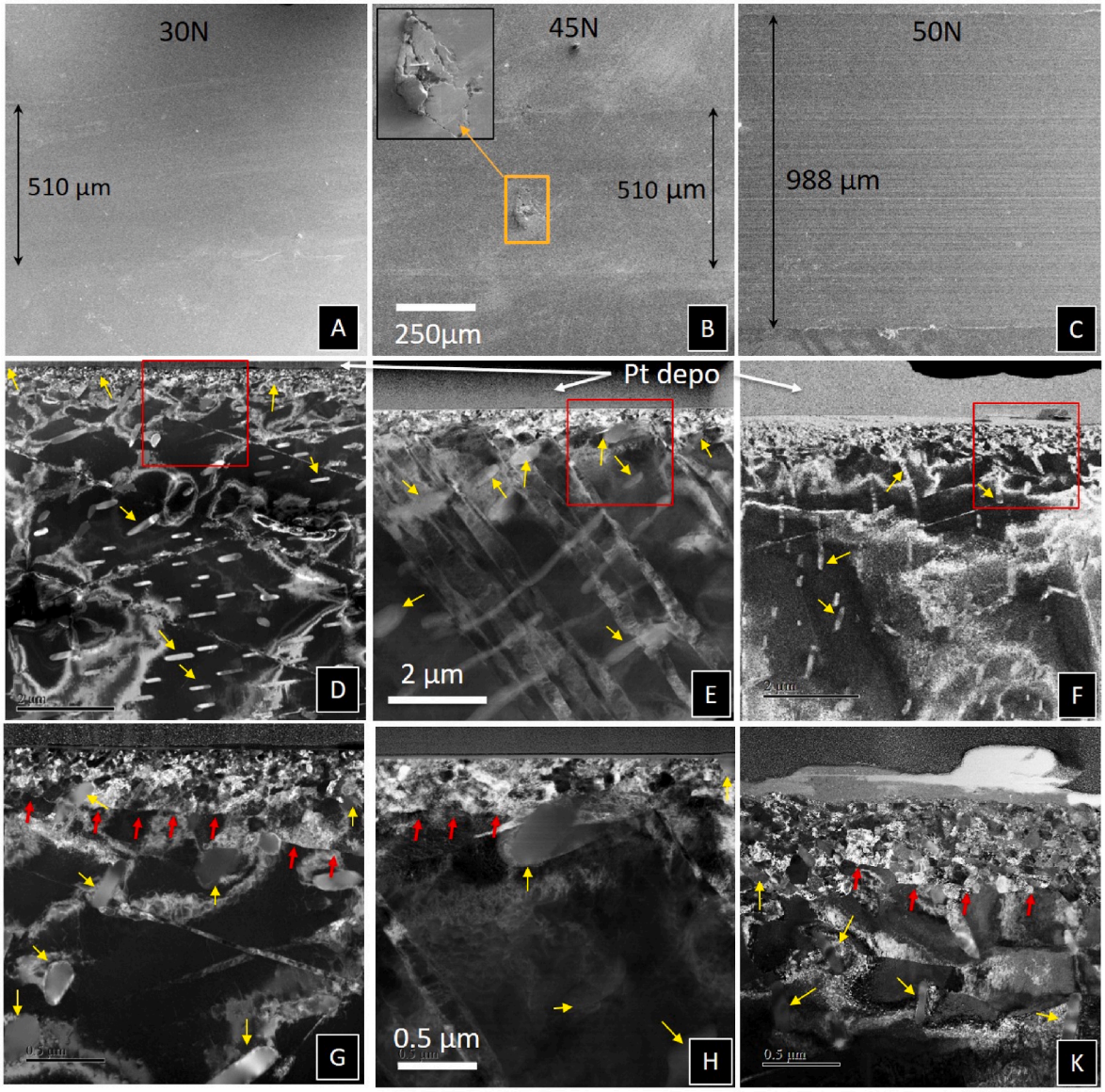

Fig. 8. SEM images (A–C) for wear tracks and STEM ADF images (D–K) for subsurface microstructure below the worn surface of 30 N (A, D & G), 45 N (B, E & H) and 50 N (C F & K). The inset in B is the crack found on the 45 N wear track, and the black arrows denote the width of the wear tracks. G, H and K are the enlarged area of the red boxes in D, E and F, respectively. White arrows indicate the Pt protection layer and surface position. Yellow arrows indicate the σ phase, and red arrows indicate the trace line between the nanocrystalline region and the bulk substrate. (For interpretation of the references to colour in this figure legend, the reader is referred to the Web version of this article.)

30 N (Figs. 8G) and 45 N (Fig. 8H). The tribolayer (greyish and bright in contrast) is observed on all three samples, and it is thin and barely visible on both 30 N and 45 N samples (Fig. 8G and H, respectively). However, it is more obvious on the 50 N sample (Fig. 8K) with a thickness of up to several hundred nanometers.

PED integrated with the TEM was used to characterize the subsurface deformation for all three samples. The scan regions for each sample are indicated by the red boxes in Fig. 8D–F. The black arrows in Fig. 9A–C shows the sliding direction and surface position. The nanocrystalline layer on the top is clearly seen on all maps. There are more small grains on the top of the 50 N sample than in the other two samples, especially shown on the GB maps (Fig. 9B, E and H). The trace lines or the interface between the nanocrystalline layer and the bulk substrates are apparent from the orientation maps (Fig. 9A, D and G). During the sliding with high contact pressure/load, the area underneath the testing surface was severely deformed, and the structures were badly damaged. Therefore, some of those structures cannot be identified in the crystal structure matching process, and these grains were marked as blank in the phase maps (Fig. 9C, F and I). All three samples are predominantly hcp phase with a small amount of fcc and σ-phase (red, green, and yellow in the phase maps, respectively). The analysis shows the proportion of the hcp phase at loads of 30 N 45 N and 50 N was similar, namely 92.8%, 92.3% and 92.7%, respectively. The percentage of fcc and σ-CoCr varies slightly from sample to sample. 50 N sample has the most fcc (5.1%) and the least σ-CoCr (2.2%) out of the three. The elongated structures are most likely the σ-phase or the mixture of fcc and σ-phase. Again, no carbides were identified on the FIB cross-sectional samples.

Fig. 10 presents EDX elemental maps of the three samples. Fig. 10a, h and o are the STEM-ADF images. Fig. 10a–g are for 30 N, Fig. 10h-n are for 45 N and Fig. 10o-u are for 50 N.

Except for the thick tribolayer and a nanocrystalline region on the 50 N sample, all three samples look similar. The finger-like or elongated features are Cr and Mo-rich compared to the matrix. Point analysis was carried out on the randomly selected points from three regions: the bulk,

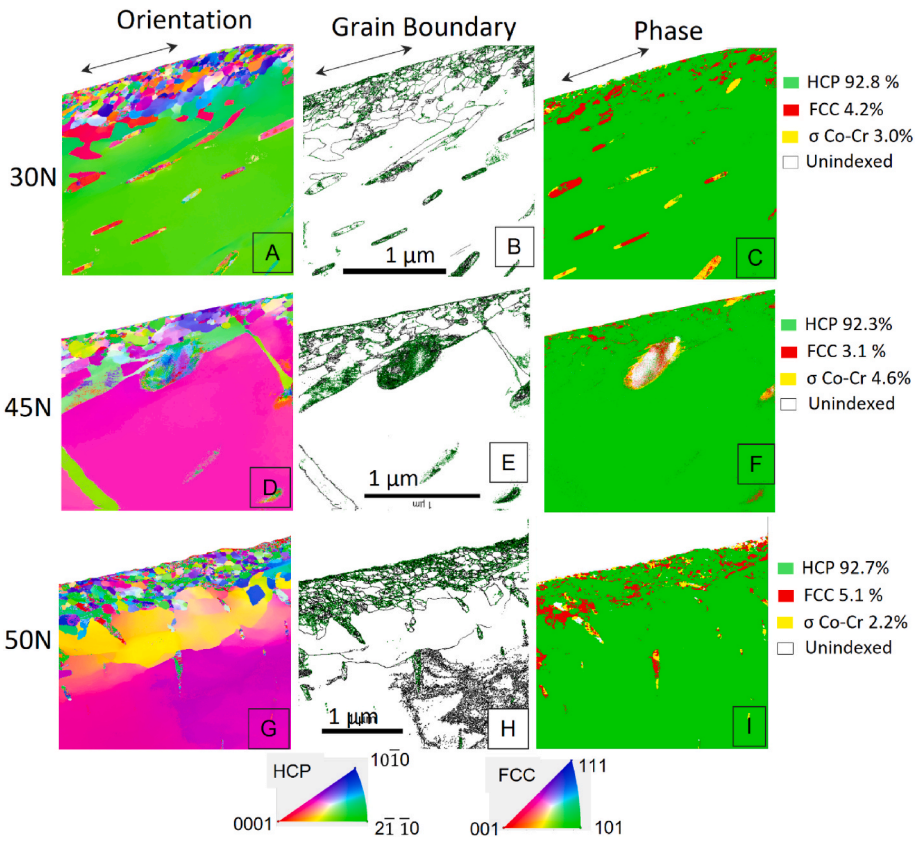

Fig. 9. PED images from cross-sections of the worn surface. Orientation, GB and phase maps of 30 N (A, B and C), 45 N (D, E and F) and 50 N (G, H and I) samples, respectively. Black arrows indicate sliding direction and the surface position. The colour keys indicate the phases and the orientation in hcp and fcc systems. (For interpretation of the references to colour in this figure legend, the reader is referred to the Web version of this article.)

particle, and surface/tribolayer. The results are presented next to the EDX maps together with the Mo and Cr to Co ratios (the last two columns of the table in Fig. 10). The composition, Mo and Cr to Co ratios of the original commercial CoCrMo sample taken from [2] and σ -CoCr taken from [29] are also presented in the table. The elongated particles are clearly Cr-rich. According to the phase diagram, σ-phase can be formed in CoCr alloys at Cr concentrations of ~54–~67% [31]. Cieslak et al. [29] reported sigma-phase $Co_{100-x}Cr_x$ with x = 57.0, 62.7 and 65.8. The corresponding Co:Cr ratios are 1.32, 1.68 and 1.92. The point EDX element analysis results show the Cr:Co ratios from all particles on the 3 samples are close to the ratio of the published σ -CoCr data [29,30]. It also noted that these particles are strongly enriched in Mo, with the Mo:Co atomic ratio amounting to 0.13–0.33 as compared to the 0.02–0.07 in the bulk. This is especially clear in the Mo elemental map in Fig. 10 g and u, which is consistent with bright/dark contrast of these particles in the Cr- and Co-based maps. Similarly, the elongated feature/stripe in Fig. S1 is seen to be enriched in Cr (Cr:Co = 1.6), Mo (Mo:Co = 0.23) and depleted of Co as compared with the bulk. The composition, Mo:Co and Cr:Co ratios in the bulk matrix of all three samples are close to the original starting material. More oxygen and carbon was found at the surface/tribolayer for 30 N and 45 N samples. The composition of the tribolayer on the 50 N sample varies from site by site (Fig. 10 o-u and S1). It is apparent that the greyish and bright contrast tribolayer (Fig. 10o) between the Pt protection layer and the substrate are different in composition (Fig. 10q, s, t and u). The bright part is oxygen-rich (Fig. 10q) and cobalt-deprived (Fig. 10t), probably a cobalt and chromium oxide mixture. The greyish part is Co and Mo-rich (Fig. 10t and u), close to the substrate in composition. The table in Fig. 10 shows this evidently, P10 and P4 in 50 N, respectively. In Fig. S1, no large oxygen-rich patch was found on the surface. However, the Cr map shows the uneven distribution of Cr across the tribolayer. It is worth pointing out that there are fractured particles embedded in the tribolayer, as indicated by the white arrows in Fig. 10s and S1, which are only seen on the 50 N sample. They have a similar chemical composition as the elongated features (P1 and P3 in Fig. S1 table).

4. Discussion

4.1. Phase identification

Phase transformation always happens after the heat treatment of CoCrMo, but with a degree of uncertainty as to the final proportion of the co-existing phases and impact that this will have on the tribological behaviour [4]. In the current work, XRD (Fig. 3C) and EBSD maps on the surface of the heat-treated sample (Figs. 3B, 5B and 6D) reveal that after the heat-treatment the dominant phase is ε-hcp, with a small amount of γ-fcc residue, and σ-CoCr with possibly some carbides ($Cr_{23}C_6$).

After scrutinizing the surface, the elongated-stripe structure with a size of a couple of hundred nanometers wide and up to several microns long has been found on the surface. The stripes observed on the cross-sectional samples are identical to those observed on the surface, as shown in Figs. 6C, 8 and 9 and 10. The stripe structure overlaps with the blue dots identified as the σ-CoCr phase when scanned at a small step by EBSD (Fig. 6D). This is further backed up by the NanoMegas data (Fig. 9), which shows that some of the stripe structures are γ-fcc, some are σ-CoCr, and some are a mixture of both. Parayil and Howell [24] reported that it was frequently observed that the σ-phase encapsulated small pools of austenite in the duplex system. Therefore, a mixture of γ-fcc and σ-CoCr is also possible. EDX results showed that these structures are Mo- and Cr-rich and Co-depleted when compared with the matrix around (Fig. 10 and S1). The point analysis on the stripes from all three samples shows that the Cr:Co ratio at these sites is very close to the

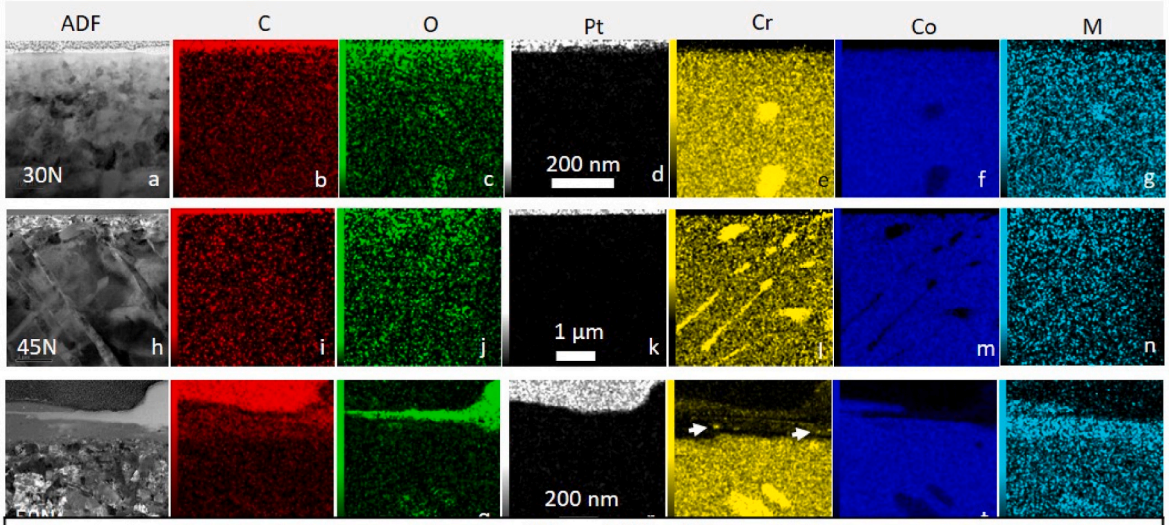

			Element (Atom%)							
		Points #	C K	O K	Cr K	Co K	Mo L	Pt M	Mo:Co	Cr:Co
30N	Particle	P1	24.03	-	41.21	30.83	3.92	-	0.13	1.34
		P2	0.42	9.86	50.27	29.64	9.81	-	0.33	1.70
	Bulk	P6	5.67	0.28	28.05	64.60	1.36	-	0.02	0.43
		P3	12.67	2.28	32.05	52.60	ND	0.40	-	0.61
	Tribolayer/ Surface	P4	41.13	11.44	10.15	28.32	3.30	5.66	0.12	0.36
		P5	35.46	20.11	9.39	32.95	ND	2.09	-	0.28
45N	Particle	P1	1.82	-	55.10	38.09	0.21	0.74	0.01	1.45
		P2	15.40	-	48.79	29.13	6.18	0.49	0.21	1.67
	bulk	P8	-	3.26	23.29	68.64	-	2.85	-	0.34
		P6	12.33	6.03	20.06	60.20	1.22	0.17	0.02	0.33
		P3	-	-	32.65	62.66	2.98	1.71	0.05	0.52
	Tribolayer/ Surface	P9	12.30	4.80	28.89	50.59	3.43	-	0.07	0.57
		P7	31.70	-	12.10	53.64	2.20	0.35	0.04	0.23
		P5	14.57	9.94	21.89	43.10	5.84	4.67	0.14	0.51
		P4	-	3.26	23.29	68.64	-	2.85	-	0.34
50N	Particle	P1	-	-	56.55	35.37	8.08	-	0.23	1.60
		P3	22.08	-	44.48	27.22	6.08	0.14	0.22	1.63
		P9	23.73	0.30	48.60	21.08	6.29	-	0.30	2.31
		P2	26.34	-	42.54	25.91	4.66	0.54	0.18	1.64
	bulk	P7	17.37	3.12	26.56	51.00	1.95	-	0.04	0.52
		P4	6.37	-	29.32	64.31	-	0.00	-	0.46
		P5	6.23	2.82	21.10	65.55	4.29	-	0.07	0.32
	Tribolayer/ Surface	P10	20.81	0.53	4.78	60.94	7.02	5.93	0.12	0.08
		P11	23.57	56.73	4.52	11.71	1.25	2.22	0.11	0.39
		P8	19.92	4.00	5.57	61.84	7.77	0.89	0.13	0.09
		P6	45.02	3.86	2.53	43.25	4.10	1.24	0.09	0.06
CoCrMo [2]					27.48	64.97	5.25		0.08	0.42
σ-CoCr [29]					57.0, 62.7, 65.8		43.0, 37.3, 34.2			1.32, 1.68, 1.92

Fig. 10. EDX element maps for subsurface cross-sectional samples at 30 N (a–g), 45 N (h–n) and 50 N (o–u). a, h and o are the STEM-ADF images for 30 N, 45 N and 50 N, respectively. EDX point analysis positions are randomly taken from 3 different regions: the bulk, on the particle and the surface/tribolayer. The atm. % of point analysis is presented in the table underneath the maps. P1, P2 etc. Refer to the site of the position where the point EDX analysis was taken.

ratio of σ-CoCr from Cieslak et al. [29]. Chung et al. [32] developed a series of dual-phase $CoCrNiMo_x$ (x = 0.4, 0.6, 0.7, 0.83 and 1.0) containing sigma and fcc phases. They reported that with the addition of Mo the formation of σ-phase was promoted. This agrees with what is widely known in stainless steel that the addition of a strong ferrite stabilizer into stainless steels (Cr, Si, or Mo) leads to the formation of the σ-phase [33]. Chung et al. [32] also reported that the content of Mo changed the fracture toughness of the alloy. With the increase of Mo, the fracture toughness was reduced. The formation of a multicomponent sigma phase could effectively mitigate the σ-phase induced embrittlement, compared with single-phase sigma. The precipitation of σ-phase found in the current study likely was promoted by the existence of Mo in the alloy. Furthermore, the elongated/stripe structure is believed to be the multicomponent sigma phase since they were enriched with both Cr and Mo, with a small variation in the content site by site. It is very hard to reach a conclusion if the embrittlement was affected or not because the percentage of Mo in this study is far lower than what was published in [32].

Given that the σ-phase is a metastable phase and the limitation of the crystal structure matching process, a further close-up observation by HRTEM was carried out (Fig. 11). Moreover, the point analysis results show that carbon content is higher in the particle and surface/tribolayer than in the bulk matrix. However, carbon contamination is so often seen on FIB samples, and it is particularly challenging to conclude if carbide

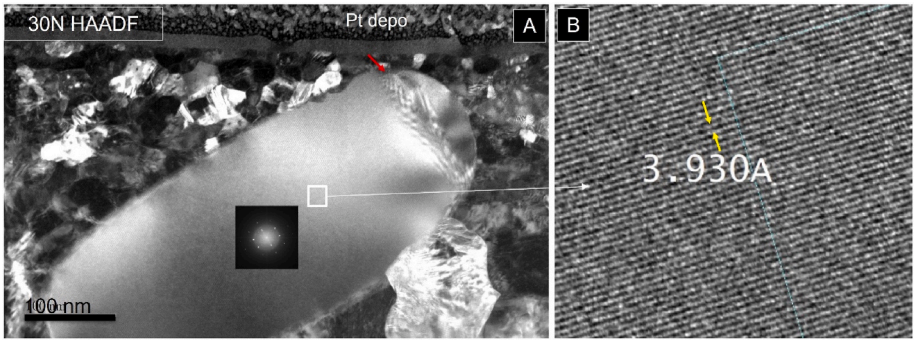

Fig. 11. A) HAADF of a single crystal of the elongated feature on 30 N sample. The inset is the diffraction pattern where it is taken. The red arrow indicates the deformation and possible fracture point on the crystal. B) HRTEM image of the fringes indicated in the white box in A. (For interpretation of the references to colour in this figure legend, the reader is referred to the Web version of this article.)

co-exists with other phases. Therefore, high-resolution TEM images on the site of the elongated particle are taken to seek further evidence.

Fig. 11 shows an intact single crystal of the elongated particle surrounded by many nano-grains (10–20 nm), which locates very close to the top surface of the 30 N sample. This crystal is 200 nm wide and 500 nm long approximately. The red arrow (Fig. 11A) indicates the deformation on the top of the crystal and a possible breakpoint on the crystal. The inset in Fig. 11A shows a diffraction pattern and the enlarged high-resolution TEM (HRTEM) image (Fig. 11B) of the area indicated by the white box in Fig. 11A. The distance between the fringes is 0.3930 nm, which agrees with the d-spacing of (210), σ -CoCr (Co7Cr8 ICSD76590) [30]. Therefore, high-resolution TEM proves further evidence that the stripe structure is indeed σ -phase.

4.2. Mechanical property of the heat-treated sample

The Vickers hardness of the as-received γ-fcc material is 397.7 ± 6.7 HV which increases up to 442.7 ± 31.8 HV after heat-treatment. The measured results are comparable to the literature [5,23,24], although as the literature shows, the hardness of CoCrMo has a wide range depending on composition and processing conditions. It also agrees with the literature that the material after heat treatment generally will have a higher hardness than before, which aligns with the fact that the starting γ-fcc dominant is softer than ε-hcp dominant after treatment [24,25].

The hardness of the as-received material was homogenous, with a small standard deviation across the surface. In contrast, after heat treatment, the hardness was relatively heterogeneous across the surface with a large standard deviation, as shown in the hardness maps in Figs. 5C and 6A. As discussed in the last section, this is due to the heterogeneous phase structure after heat treatment. The σ-phase is documented to improve the hardness and wear performance of the material [16,24,25,35,36]. This in line with the maps in Fig. 6, where γ-fcc (red) is softer than the ε-hcp (green) and σ (blue). However, the mean values of the hardness from the Vickers test are far lower than that from the nanoindentation tests. This is partly because of the different measurement methods employed. The other reason is the highly heterogeneous surface. The results will differ when the test is carried out in a relatively small region compared with a large area.

There are extensive reports about the mechanical properties of the σ-phase, often from duplex stainless steels [20,21,37,38], but also from CoCr alloys containing σ -CoCr [34,39,40]. However, such measurements are often derived from regions that have been a combination of different phases [4,7], and there are no reports where the mechanical properties were obtained uniquely from the σ-phase in the CoCr system. PF_QNM measurements were used to acquire local mechanical properties of the ε-hcp and σ-CoCr, as shown in Fig. 8. The bright stripe structure in Fig. 6A and C are confirmed to be the σ-CoCr in Fig. S3. In the EDX maps, the bright stripes are Mo- and Cr-rich and Co-deplete and overlap with the blue dots indexed as σ -CoCr. Compared with ε-hcp in the matrix, the σ-phase has a high modulus of at least twice that of the ε-hcp. Young's modulus is proportional to hardness regardless of the material. Therefore, the hardness of the σ-phase is at least twice that of ε-hcp. This agrees with Maehara et al. [38] who reported that the Vickers hardness in the blocky σ-phase is about 900–1000 HV, about 260 HV in the fine ferrite phase and 230 HV for austenite.

4.3. Wear transition

The 30 N exhibited the lowest wear rate (Fig. 1) with the most stable and highest potential of all tests (Fig. 2). The highest potential indicates the most passivated surface, and therefore an effective protection layer must have formed on the surface. This layer is not so apparent from TEM images (Fig. 9A, D), but a thin oxide/carbon based layer is seen from the ADF images and EDX carbon and oxygen maps (Fig. 9a–c). The protective layer formation has been reported widely [2,4]. With the formation of the protective layer, the friction performance and wear resistance significantly improve.

The sudden more than 5-fold wear transition (Fig. 1) when the load/contact pressure increases from 45 N (3.6 GPa) to 50 N (3.7 GPa) is almost certainly induced by the sudden break down of the hard but brittle σ-phase due to the increased contact stresses. It is known that a reduction in the amount and size of the σ-phase will enhance ductility [16], while only the precipitation of even a tiny amount of σ-phase decreases the impact strength significantly [38]. As indicated by the red arrow in Fig. 11A, the start of fracture of the σ-phase is seen at 30 N, with more extensive cracking in the 45 N wear track (Fig. 8B). However, at these loads, the σ –phase still remains bonded to the matrix. However, when the load reaches 50 N, the fracture of the brittle σ-particles leads to particle detachment and the introduction of third-body wear, which leads to significant increases in wear rate. The break-up of the σ-phase at 50 N is clearly observed from the phase maps in Fig. 9I, where the large and intact σ-particles are barely seen near the top surface compared to the images from 30 N to 45 N (Fig. 9C and F, respectively). A thick tribolayer was seen on the 50 N sample but not on other lower-load samples. The fractured σ-particles are visibly embedded in both the heavily deformed nanocrystalline region and the tribolayer on the 50 N sample (Fig. 8 F and K, 9 F, 10s and S2). Furthermore, simultaneously, the crushed fragments of the hard σ-particles, serving as the third-body, rapidly damage the surface structure and remove the surface material when sliding across the surface, contributing heavily to the wear increase. The mean CoFs at 45 N increased from 0.082 to 0.120 at 50 N (Fig. 2C), providing evidence for this observation The evidence also comes from the thick but not uniform tribolayer on 50 N sample. As shown in Fig. 8F, K, 10 o-p and S2, this tribolayer is not uniform both in thickness and chemical composition. This is the result of the synergistic effects of severe mechanical mixing and corrosion. However, this tribolayer failed to provide effective protection for the surface in two ways. Firstly, the Cr oxide only partially covers the surface, with the other

parts covered by the mixture of Co and Mo (Fig. 10q, s, t, u and S2). The Cr-depleted area will be corroded preferentially. This explains that the OCP of the 50 N sample reduces significantly down to −0.55 V and stays around −0.5 V for a while after a quick recovery after running-in, while the OCPs for other lower load samples stay above −0.4 V (Fig. 2B) after the quick dip. Secondly, the embedded hard fragments of σ-particles, which are loosely scattered within the tribolayer, can severely damage the surface structure underneath it. This ends up with the thick nanocrystalline layer on the subsurface (Fig. 8F and G). Both factors play a part in the abrupt wear rate increase.

A similar wear transition was observed by Namus et al. [2] for the same alloy but in the fcc γ-phase state. Fig. 12 gives a comparison of the wear transition observed here and that reported by Namus et al. [2]. In the pre-transition region, the wear rate of the hcp ε-phase, with σ-precipitation, CoCrMo alloy was slightly higher than the fcc structure. A reduction in corrosion resistance is another well-known property of the σ -phase [29,33,41]. As discussed in previous sections, the σ-phase is enriched Cr, which means that formation of σ-phase results in a Cr-depleted zone around it, which leads to the reduction in corrosion resistance. In stainless steel, the presence of σ-phase and γ-austenite induce a galvanic effect, and the γ-austenite is corroded preferentially [11]. In the present work, we believe that with the formation of σ-phase in the heat-treated samples also reduced the corrosion resistance because of the Cr-depleted regions. This leads to the result that the wear rates of the heat-treated sample in the pre-transition region are slightly higher than that of the counterpart fcc alloy at the same test conditions.

The load at which the wear transition occurs was lower for the hcp structure compared to the fcc structure. As noted above, this is related to the fracture of the σ-CoCr particles in the hcp material. It also coincides with the formation of a nanocrystalline layer being formed. The same was observed for the fcc alloy reported in [2]. These nanocrystalline layers are a result of the limited deformation modes in these low stacking fault energy materials that results shear banding to accommodate the imposed strain. Such nanocrystalline layers are commonly observed in CoCrMo and other similar low stacking fault energy alloys, as discussed in [2].

Post transition wear rates were similar for both materials. The higher pre-transition wear rate for the hcp material contrasts with the work of Saldívar-García and López [6], who observed significantly lower wear rates for the hcp in a direct comparison with the fcc. However, these authors did not make a detailed analysis of the microstructure and therefore, it is unclearer whether any σ-phase was present. Interestingly, Balagna et al. [42] also failed to find a significant difference between the hcp and fcc forms in CoCrMo. Zhao et al. [16] did find an improvement in wear behaviour in a hcp alloy which contained σ-CoCr, but which had a very fine grain size, and the σ-CoCr was present as nanoscale particles, which does not provide a fair comparison to the current work. Further work is required to define the wear behaviour of the hcp structure without the complication of the σ-phase.

5. Conclusions

- After heat treatment the ε-hcp is the dominant matrix phase, with a small amount of γ-hcp and σ-phase.
- PF_QNM measurement was used to acquire local mechanical properties of the ε-hcp and σ-phase. σ -Phase has a very high modulus of at least twice that of the ε-hcp.
- An abrupt wear transition (5-fold) was observed when the load increased from 45 N (3.6 GPa) to 50 N (3.7 GPa). The wear transition is almost certainly induced by the sudden breakdown of the relatively hard but brittle σ-phase due to the increased force/pressure.

Author contributions

J.Q.: Conceptualization, Investigation, Data Curation, Formal analysis, Writing -Original draft. W.M.R: Funding acquisition, Supervision, Validation, Writing - Reviewing & Editing. L.M: Investigation. P.G. Investigation. All authors reviewed the manuscript.

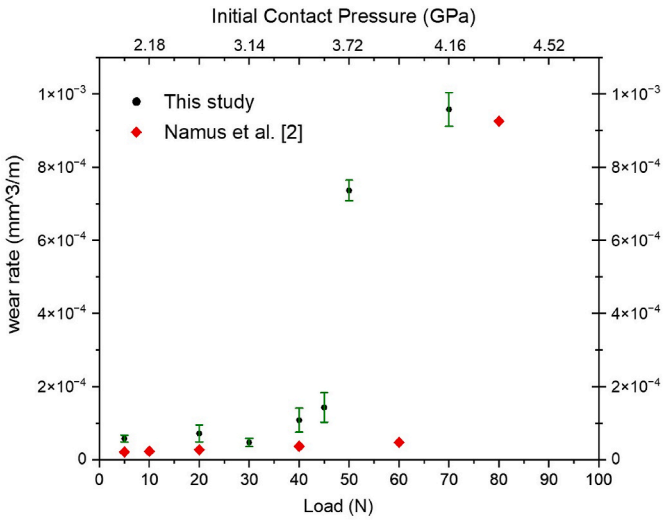

Fig. 12. Comparison of the wear rates observed in the current work compared to those for the same material, but with an FCC structure, observed by Namus et al. [2].

Declaration of competing interest

The authors declare that they have no known competing financial interests or personal relationships that could have appeared to influence the work reported in this paper.

Data availability

The raw and processed data required to reproduce these findings are available to download from the link at the attach file step.

Acknowledgement

This work is supported by the Engineering and Physical Sciences Research Council (grant number EP/001766/1) as a part of 'Friction: The Tribology Enigma' Programme Grant (www.friction.org.uk), a collaboration between the Universities of Leeds and Sheffield.

The authors wish to acknowledge the Henry Royce Institute for Advanced Materials, funded through EPSRC grants EP/R00661×/1, EP/S019367/1, EP/P02470×/1 and EP/P025285/1, for access to the JEOL JEM-F200, Bruker TriboLab, JEOL JEM 7900 F and Bruker Dimension XR through Royce@Sheffield.

Appendix A. Supplementary data

Supplementary data to this article can be found online at https://doi.org/10.1016/j.wear.2023.204649.

References

[1] L. Kunčická, R. Kocich, T.C. Lowe, Advances in metals and alloys for joint replacement, Prog. Mater. Sci. 88 (2017) 232–280, https://doi.org/10.1016/j.pmatsci.2017.04.002.

[2] R. Namus, P. Zeng, W.M. Rainforth, Correlation of the wear transition in CoCrMo alloys with the formation of a nanocrystalline surface layer and a proteinaceous surface film, Wear 376 (377) (2017) 223–231, https://doi.org/10.1016/j.wear.2016.11.046.

[3] R.J. Narayan (Ed.), Materials for Medical Devices, ASM International, 2012, https://doi.org/10.31399/asm.hb.v23.9781627081986.

[4] S. Zangeneh, H.R. Lashgari, A. Roshani, Microstructure and tribological characteristics of aged Co – 28Cr – 5Mo – 0 . 3C alloy, Mater. Des. 37 (2012) 292–303, https://doi.org/10.1016/j.matdes.2011.12.041.

[5] A.J.T. Clemow, B.L. Daniell, The influence of microstructure on the adhesive wear resistance of a Co-Cr-Mo alloy, Wear 61 (2) (Jun. 1980) 219–231, https://doi.org/10.1016/0043-1648(80)90287-2.

[6] A.J. Saldívar-García, H.F. López, Microstructural effects on the wear resistance of wrought and as-cast Co-Cr-Mo-C implant alloys, J. Biomed. Mater. Res., Part A 74A (2) (Aug. 2005) 269–274, https://doi.org/10.1002/jbm.a.30392.

[7] H.S. Dobbs, J.L.M. Robertson, Heat treatment of cast Co-Cr-Mo for orthopaedic implant use, J. Mater. Sci. 18 (2) (Feb. 1983) 391–401, https://doi.org/10.1007/BF00560627.

[8] H.R. Lashgari, S. Zangeneh, F. Hasanabadi, M. Saghafi, Microstructural evolution during isothermal aging and strain-induced transformation followed by isothermal aging in Co-Cr-Mo-C alloy: a comparative study, Mater. Sci. Eng., A 527 (16–17) (2010) 4082–4091, https://doi.org/10.1016/j.msea.2010.03.018.

[9] D.L. Klarstrom, Heat treatment of cobalt-base alloys, in: G.E. Totten, D. S. MacKenzie (Eds.), ASM Handbook, 4E, ASM International, 2016, pp. 625–633, https://doi.org/10.31399/asm.hb.v04e.a0006267.

[10] M. Niinomi, Co–Cr-based alloys, in: Structural Biomaterials, Elsevier, 2021, pp. 103–126, https://doi.org/10.1016/B978-0-12-818831-6.00006-9.

[11] P. Huang, H.F. López, Effects of grain size on development of athermal and strain induced ϵ martensite in Co–Cr–Mo implant alloy, Mater. Sci. Technol. 15 (2) (Feb. 1999) 157–164, https://doi.org/10.1179/026708399101505699.

[12] T. Nakano, K. Hagihara, A.R. Ribeiro, Y. Fujii, T. Todo, R. Fukushima, L.A. Rocha, Orientation dependence of the wear resistance in the Co–Cr–Mo single crystal, November 2020, Wear 478–479 (2021), 203758, https://doi.org/10.1016/j.wear.2021.203758.

[13] P. Khaimanee, P. Choungthong, V. Uthaisangsuk, Effects of isothermal aging on microstructure evolution, hardness and wear properties of wrought Co-Cr-Mo alloy, J. Mater. Eng. Perform. 26 (3) (2017) 955–968, https://doi.org/10.1007/s11665-017-2525-x.

[14] J. Cawley, J.E.P. Metcalf, A.H. Jones, T.J. Band, D.S. Skupien, A Tribological Study of Cobalt Chromium Molybdenum Alloys Used in Metal-On-Metal Resurfacing Hip Arthroplasty, 255, 2003, pp. 999–1006, https://doi.org/10.1016/S0043-1648(03)00046-2.

[15] Y. Liao, R. Pourzal, P. Stemmer, M.A. Wimmer, J.J. Jacobs, A. Fischer, L.D. Marks, New insights into hard phases of CoCrMo metal-on-metal hip replacements, J. Mech. Behav. Biomed. Mater. 12 (Aug. 2012) 39–49, https://doi.org/10.1016/j.jmbbm.2012.03.013.

[16] C. Zhao, J. Zhou, Q. Mei, F. Ren, Microstructure and dry sliding wear behavior of ultrafine-grained Co-30 at% Cr alloy at room and elevated temperatures, J. Alloys Compd. 770 (2019) 276–284, https://doi.org/10.1016/j.jallcom.2018.08.092.

[17] K. Asgar, F.A. Peyton, Effect of microstructure on the physical properties of cobalt-base alloys, J. Dent. Res. 40 (1) (Jan. 1961) 63–72, https://doi.org/10.1177/00220345610400012501.

[18] G. Restrepo Garcés, J. Le Coze, J.L. Garin, R.L. Mannheim, σ-phase precipitation in two heat-resistant steels - influence of carbides and microstructure, Scripta Mater. 50 (5) (2004) 651–654, https://doi.org/10.1016/j.scriptamat.2003.11.021.

[19] M.J. Perricone, T.D. Anderson, C.V. Robino, J.N. DuPont, J.R. Michael, Effect of composition on the formation of sigma during single-pass welding of Mo-bearing stainless steels, Metall. Mater. Trans. A Phys. Metall. Mater. Sci. 38 A (9) (2007) 1976–1990, https://doi.org/10.1007/s11661-007-9158-x.

[20] S.K. Ghosh, S. Mondal, High temperature ageing behaviour of a duplex stainless steel, Mater. Char. 59 (12) (2008) 1776–1783, https://doi.org/10.1016/j.matchar.2008.04.008.

[21] T.H. Chen, J.R. Yang, Effects of solution treatment and continuous cooling on σ-phase precipitation in a 2205 duplex stainless steel, Mater. Sci. Eng., A 311 (1–2) (2001) 28–41, https://doi.org/10.1016/S0921-5093(01)00911-X.

[22] H. Sieurin, R. Sandström, Sigma phase precipitation in duplex stainless steel 2205, Mater. Sci. Eng., A 444 (1–2) (2007) 271–276, https://doi.org/10.1016/j.msea.2006.08.107.

[23] M.R. El Koussy, I.S. El Mahallawi, W. Khalifa, M.M. Al Dawood, M. Bueckins, Effects of thermal aging on microstructure and mechanical properties of duplex stainless steel weldments, Mater. Sci. Technol. 20 (3) (Mar. 2004) 375–381, https://doi.org/10.1179/174328413X13789824293821.

[24] T.R. Parayil, P.R. Howell, Decomposition of deformed ferrite in a duplex stainless steel, Mater. Sci. Technol. 2 (11) (1986) 1131–1139, https://doi.org/10.1179/mst.1986.2.11.1131.

[25] Y. Chen, Y. Li, S. Kurosu, K. Yamanaka, N. Tang, Y. Koizumi, A. Chiba, Effects of sigma phase and carbide on the wear behavior of CoCrMo alloys in Hanks' solution, Wear 310 (1–2) (2014) 51–62, https://doi.org/10.1016/j.wear.2013.12.010.

[26] G.M. Pharr, An improved technique for determining hardness and elastic modulus using load and displacement sensing indentation experiments, J. Mater. Res. 7 (6) (Jun. 1992) 1564–1583, https://doi.org/10.1557/JMR.1992.1564.

[27] Y. Hua, PeakForce-QNM Advanced Applications Training 2014, 2014 [Online]. Available: https://mmrc.caltech.edu/AFM Dimension Icon/Bruker Training/PeakForce QNM_Adv Apps Training 2014.pdf.

[28] Bruker Corporation, PeakForce QNM - User Guide, 2010, p. 84 [Online]. Available: https://mmrc.caltech.edu/AFM Dimension Icon/Bruker Training/004-1036-000 PEAKFORCE QNM USERS GUIDE-F.pdf.

[29] J. Cieslak, S.M. Dubiel, M. Reissner, Site occupancy and lattice parameters in sigma-phase Co-Cr alloys, Acta Crystallogr. Sect. B Struct. Sci. 68 (2) (2012) 123–127, https://doi.org/10.1107/S0108768112006234.

[30] G.J. Dickins, A.M.B. Douglas, W.H. Taylor, The crystal structure of the Co–Cr σ phase, Acta Crystallogr. 9 (3) (Mar. 1956) 297–303, https://doi.org/10.1107/S0365110X56000826.

[31] K. Ishida, T. Nishizawa, The Co-Cr (Cobalt-Chromium) system, Bull. Alloy Phase Diagrams 11 (4) (Aug. 1990) 357–370, https://doi.org/10.1007/BF02843315.

[32] D.H. Chung, X.D. Liu, Y. Yang, Fracture of sigma phase containing Co–Cr–Ni–Mo medium entropy alloys, J. Alloys Compd. 846 (Dec. 2020), 156189, https://doi.org/10.1016/j.jallcom.2020.156189.

[33] C.-C. Hsieh, W. Wu, Overview of intermetallic sigma ( ) phase precipitation in stainless steels, 2012, ISRN Metall (4) (2012) 1–16, https://doi.org/10.5402/2012/732471.

[34] B. Henriques, A. Bagheri, M. Gasik, J.C.M. Souza, O. Carvalho, F.S. Silva, R. M. Nascimento, Mechanical properties of hot pressed CoCrMo alloy compacts for biomedical applications, Mater. Des. 83 (2015) 829–834, https://doi.org/10.1016/j.matdes.2015.06.069.

[35] G. Cornacchia, S. Cecchel, D. Battini, C. Petrogalli, A. Avanzini, Microstructural, mechanical, and tribological characterization of selective laser melted CoCrMo alloy under different heat treatment conditions and hot isostatic pressing, Adv. Eng. Mater. 24 (4) (2022), https://doi.org/10.1002/adem.202100928.

[36] M.H. Tsai, H. Yuan, G. Cheng, W. Xu, W.W. Jian, M.-H. Chuang, C.-C. Juan, A.-C. Yeh, S.-J. Lin, Y. Zhu, Significant hardening due to the formation of a sigma phase matrix in a high entropy alloy, Intermetallics 33 (2013) 81–86, https://doi.org/10.1016/j.intermet.2012.09.022.

[37] I. Zucato, M.C. Moreira, I.F. Machado, S.M.G. Lebrão, Microstructural characterization and the effect of phase transformations on toughness of the UNS S31803 duplex stainless steel aged treated at 850 °C, Mater. Res. 5 (3) (2002) 385–389, https://doi.org/10.1590/s1516-14392002000300026.

[38] Y. Maehara, M. Koike, N. Fujino, T. Kunitake, Precipitation of sigma phase in a 25Cr-7Ni-3Mo duplex phase stainless steel, Trans. Iron Steel Inst. Japan 23 (3) (1983) 240–246, https://doi.org/10.2355/isijinternational1966.23.240.

[39] Y. Sato, N. Nomura, S. Fujinuma, A. Chiba, Microstructure and tensile properties of hot-pressed Co-Cr-Mo alloy compacts for biomedical applications, Nippon Kinzoku Gakkaishi/Journal Japan Inst. Met. 72 (7) (2008) 532–537, https://doi.org/10.2320/jinstmet.72.532.

[40] N. Nomura, M. Abe, A. Kawamura, S. Fujinuma, A. Chiba, N. Masahashi, S. Hanada, Fabrication and mechanical properties of porous Co–Cr–Mo alloy compacts without Ni addition, Mater. Trans. 47 (2) (2006) 283–286, https://doi.org/10.2320/matertrans.47.283.

[41] E.O. Hall, S.H. Algie, The sigma phase, Metall. Rev. 11 (1) (Jan. 1966) 61–88, https://doi.org/10.1179/mtlr.1966.11.1.61.

[42] C. Balagna, S. Spriano, M.G. Faga, Characterization of Co–Cr–Mo alloys after a thermal treatment for high wear resistance, Mater. Sci. Eng. C 32 (7) (Oct. 2012) 1868–1877, https://doi.org/10.1016/j.msec.2012.05.003.